Not all voxels are created equal: reducing estimation bias in regional NODDI metrics using tissue-weighted means

Parker CS[1†*], Veale T[2,3†], Bocchetta, M[2], Slattery CF[2], Malone, IB[2], Thomas, DL[2,4,5], Schott JM[2], Cash DM[1,2,3‡], Zhang H[1‡]

[1]Centre for Medical Image Computing, Department of Computer Science, UCL, London, UK

[2]The Dementia Research Centre, Department of Neurodegenerative Disease, UCL Queen Square Institute of Neurology, UCL, London, UK

[3]UK Dementia Research Institute at UCL, UCL, London, UK

[4]Department of Brain Repair and Rehabilitation, UCL Queen Square Institute of Neurology, UCL, London, UK

[5]Wellcome Centre for Human Neuroimaging, UCL Queen Square Institute of Neurology, UCL, London, UK

[†] Joint first authors

[‡] Joint senior authors

* Corresponding author: christopher.parker@ucl.ac.uk. University College London, Centre for Medical Image Computing, 90 High Holborn, Floor 1, London, UK, WC1V6LJ

Declarations of interest: None

Abstract

Neurite orientation dispersion and density imaging (NODDI) estimates microstructural properties of neurites relating to their organisation and processing capacity that are essential for effective neuronal communication. Descriptive statistics of NODDI tissue metrics are commonly analysed in regions-of-interest (ROI) to identify brain behaviour associations. Here, the conventional method to calculate the ROI mean weights all voxels equally. However, this produces biased estimates in the presence of CSF partial volume. This study introduces the tissue-weighted mean, which calculates the mean NODDI metric across the tissue within an ROI, utilising the tissue fraction estimate from NODDI to reduce estimation bias. We demonstrate the proposed mean in a study of white matter abnormalities in young onset Alzheimer's disease (YOAD). Results show the conventional method induces significant bias that correlates with CSF partial volume, primarily affecting periventricular regions and more so in YOAD subjects than in healthy controls. The tissue-weighted mean robustly identified disease-related differences in ROIs such as the fornix (p<0.05, Bonferroni corrected), some of which were absent using the conventional mean. The tissue-weighted mean may generate new insight into microstructural disease-related effects in regions typically confounded by partial volume, representing a promising tool for the study of microstructural correlates of aging and neurodegenerative diseases.

1. Introduction

Neurite orientation dispersion and density imaging (NODDI) is a widely used approach for estimating microstructural properties of tissue (Zhang, H. et al 2012) using diffusion weighted magnetic resonance imaging (DWI) (Alexander et al 2019). NODDI estimates the density and orientation dispersion of neurites, two key aspects of neurite morphology. These tissue metrics, termed neurite density index (NDI) and orientation dispersion index (ODI), relate to the density and structural organisation of axons in white matter and dendrites in grey matter that are essential for neural communication and provide useful biomarkers of brain function. Their changes have been linked to function in both healthy populations (Kunz et al 2014, Genc et al 2018, Mollink et al 2019) and in cases of diseases (Winston et al 2014, Broad et al 2019, Scahill et al 2020).

A common way of investigating NODDI tissue metrics is region-of-interest (ROI) analysis. This utilises descriptive statistics of NODDI metrics in ROIs to summarise microstructure in a region. These statistics may then be correlated to neurological phenotypes in order to make inferences about brain-behaviour associations. This approach has been applied in studies of normal development (Lynch et al 2020), aging (Kodiweera et al 2016) and in neurological diseases such as Huntington's disease (Zhang, J. et al 2018, Scahill et al 2020), fronto-temporal dementia (Wen, J. et al 2019) and Alzheimer's diseases (Colgan et al 2016, Slattery et al 2017, Parker et al 2018, Wen, Q. et al 2019).

A typically used descriptive statistic is the mean of NODDI tissue metrics in an ROI, such as mean NDI or ODI. Conventional methods calculate this by averaging NODDI tissue metrics across all voxels in an ROI (Parker et al 2018, Zhang, J. et al 2018, Wen, J. et al 2019, Wen, Q. et al 2019, Andica et al 2020, Scahill et al 2020). However, weighting all voxels equally does not account for the fact that the amount of tissue present in a voxel can vary within a region due to partial volume induced by cerebrospinal fluid (CSF) contamination (Vos et al 2011, Metzler-Baddeley et al 2012). This can lead to a mis-estimation of the mean microstructure of the tissue across the ROI, which can be problematic for white matter tracts in periventricular regions whose border are particularly vulnerable to containing high CSF partial volume. Given that ventricular enlargement is a prominent feature in individuals with Alzheimer's disease (Schott et al., 2005), NODDI data from these patients are more likely to be affected by this issue.

In order to avoid this problem, previous approaches have aimed to estimate ROI means from voxels with minimal partial volume. For example, by applying the conventional mean to tract centres that can be reconstructed from tract-based spatial statistics (Kodiweera et al 2016, Slattery et al 2017, Andica et al 2019), or a weighted mean to region streamline density (Lynch et al 2020). However, these techniques may not be effective for

thin periventricular regions, such as the fornix, whose tract width is of similar magnitude to the size of DWI voxels. Most importantly, neither can fully capture the average tissue metric across a region.

To address this, we introduce the tissue-weighted mean, a new approach that aims to produce unbiased estimates of regional microstructure. The key idea is to utilise tissue fraction (TF) metrics from NODDI to explicitly account for CSF partial volume in ROI voxels. This is enabled by NODDI's explicit representation of the tissue and CSF compartments. In contrast to the previous approaches, this permits usage of the full tissue microstructural information across the ROI. Tissue-weighted means therefore aim to account for partial volume while retaining the intent of the conventional means.

This study aims to evaluate the estimation bias associated with conventional ROI means and to assess the impact of applying the tissue-weighted mean to studies of neurodegenerative disease. To do this, we provide an example of applying the tissue-weighted mean to study white matter abnormalities in Young Onset Alzheimer's Disease (YOAD). Bias in conventional means is quantified and effect sizes for group differences are compared between the two approaches.

The rest of this paper is organised as follows: we first formally define the tissue-weighted mean, before explaining the theory and methods used to quantify bias in conventional means. We then describe the methods for calculating conventional and tissue-weighted means of NODDI tissue metrics in a cohort consisting of cognitively healthy individuals and those with YOAD. Bias in conventional means and differences in effect sizes are compared and reported across all ROIs. Finally, we discuss the anatomical plausibility of group differences identified using the tissue-weighted mean and the implications of findings for previous studies.

2. Theory

2.1. NODDI model: voxel compartments and tissue parameters

NODDI adopts a multi-compartment model of the diffusion signal in each voxel (Zhang, H. et al 2012). The model assumes the DWI signal is a summation of signals from two primary compartments in a voxel: one representing free water and the other from tissue (Fig. 1). The free water fraction (FWF) parameter estimates the volume fraction of free water, contributed primarily from CSF. The TF parameter estimates the volume fraction of the tissue, TF=1-FWF.

Further parameters are derived corresponding to properties of the intra-neurite and extra-neurite space within the tissue component of the voxel. NDI provides a surrogate measure of the neurite density in the tissue compartment and ranges from 0 (low density) to 1 (high density). ODI estimates the dispersion of neurite orientations in the tissue and ranges from 0 (no dispersion) to 1 (fully dispersed).

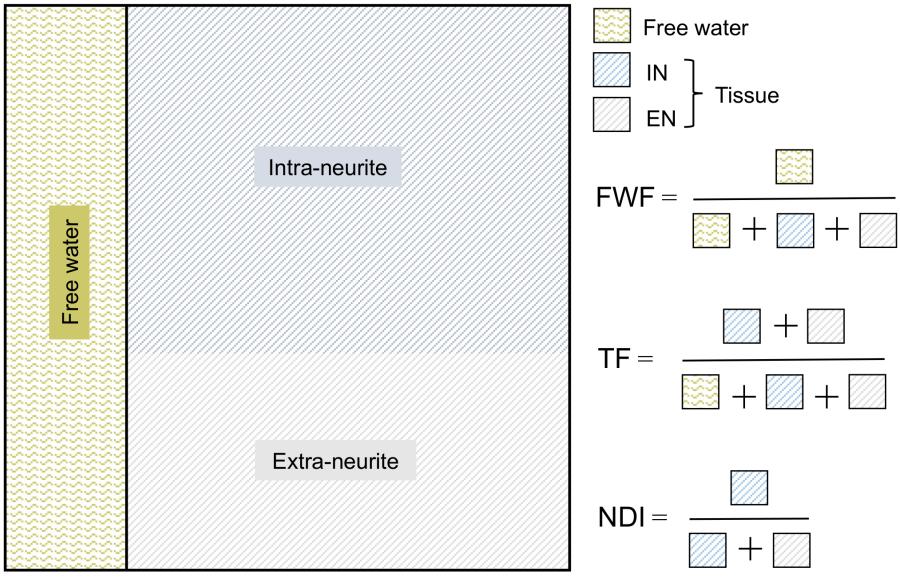

Figure 1. Graphical representation of the NODDI model. The model estimates the volume of the free water (area shaded with wiggly lines) and tissue (area shaded with straight lines) compartments within a voxel, parameterised as the free water fraction (FWF) and tissue fraction (TF), respectively. The tissue volume is further represented as two sub-compartments, each estimating the volume of the intra-neurite (IN) and extra-neurite space (EN) (lines coloured blue and grey, respectively). NDI estimates the density of intra-neurite space within the tissue and is equal to the relative volume fraction of the intra-neurite

compartment. ODI is also a property of the tissue, representing the orientational distribution of the intra-neurite space.

2.2. Conventional mean

The conventional mean of NDI or ODI weighs each voxel equally and is calculated as the arithmetic mean. Let m denote the set of values for a NODDI tissue property of interest (i.e. NDI or ODI) in an ROI. Its arithmetic mean, denoted as $\bar{\mathrm{m}}$, is then

$$\bar{\mathrm{m}} = \frac{1}{\mathrm{N}} \sum_{\mathrm{i}=1}^{\mathrm{N}} \mathrm{m}_{\mathrm{i}} \ , \tag{1}$$

where i is the voxel index within the ROI, ranging from 1 to N, the number of voxels in the ROI. m_{i} is the NODDI tissue property for voxel i.

2.3. Tissue-weighted mean

The tissue-weighted mean instead calculates the mean of the metric across the tissue component of the ROI using a weighted average, with the weightings being the fraction of tissue in each voxel. The tissue-weighted mean of m, denoted as $\bar{\mathrm{m}}_{\mathrm{t}}$, is thus:

$$\bar{\mathrm{m}}_{\mathrm{t}} = \frac{\sum_{\mathrm{i}=1}^{\mathrm{N}} \mathrm{t}_{\mathrm{i}}\, \mathrm{m}_{\mathrm{i}}}{\sum_{\mathrm{i}=1}^{\mathrm{N}} \mathrm{t}_{\mathrm{i}}}, \tag{2}$$

where t_{i} is the TF of voxel i within the ROI. This is equivalent to

$$\bar{\mathrm{m}}_{\mathrm{t}} = \frac{\overline{\mathrm{tm}}}{\bar{\mathrm{t}}}, \tag{3}$$

a more concise formulation derived by dividing both the numerator and denominator of equation (2) by N.

2.4. Bias in conventional means

Fig. 2 shows an illustrative example of calculating the two means in an ROI consisting of two voxels, each with different TFs. When calculating the conventional mean, NDI values in the voxel with lower TF are overweighted, resulting in a miscalculation of the tissue mean. In contrast, the tissue-weighted mean weights each NDI value by its voxel TF

and gives correct calculations of the tissue mean. This demonstrates that the conventional mean is in general a biased estimate of the tissue-weighted mean.

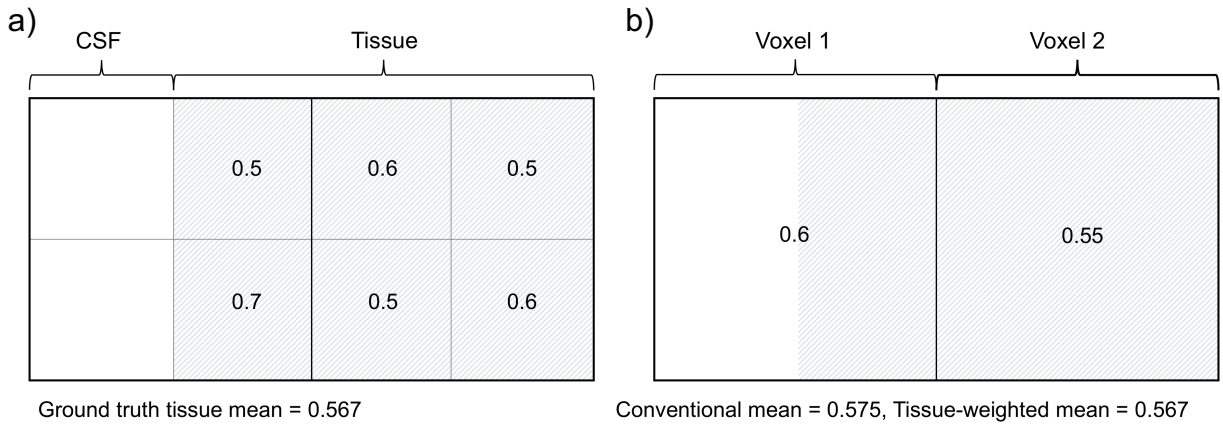

Figure 2. Illustrative case of estimation bias in the conventional mean in an ROI consisting of two voxels with different tissue volumes. a) Shows an ROI covering an area of ground truth anatomy containing both CSF and tissue. Numbers in each sub-region show the local neurite density and are approximately normally distributed. b) Shows NODDI tissue parameter of NDI in two voxels covering the ROI. For each voxel, the NDI parameter describes the average neurite density of the tissue sub-regions that the voxel covers. In the presence of CSF partial volume, the conventional mean misestimates the ground truth mean by overweighting the NDI value in voxel 1, generating a bias of 0.008. Using estimates of the TF to weight the NDI in each voxel, the tissue-weighted mean correctly calculates the mean NDI of the tissue as 0.567.

To clearly show the relation between the two means, observe that the numerator in equation (3) can be written as

$$\overline{tm} = \frac{1}{N}\sum_{i=1}^{N}\big((t_i - \bar{t}) + \bar{t}\big)\big((m_i - \bar{m}) + \bar{m}\big), \tag{4}$$

which simplifies to

$$\overline{tm} = \bar{t}\,\bar{m} + \mathrm{Cov}(m, t), \tag{5}$$

where $\mathrm{Cov}(\mathrm{m},\mathrm{t})$ is the covariance of m and t across the ROI. Here, $\mathrm{Cov}(\mathrm{m},\mathrm{t})$ is calculated without Bessel's correction (with N instead of N-1 in the denominator), which is an unbiased estimate of the population covariance when N is large.

Dividing equation (5) by $\bar{\mathrm{t}}$ shows that the tissue-weighted mean is the conventional mean with an additional term, namely the covariance of m and t divided by $\bar{\mathrm{t}}$. The difference between the means can be written as

$$\bar{\mathrm{m}} - \bar{\mathrm{m}}_{\mathrm{t}} = -\frac{\mathrm{Cov}(\mathrm{m},\mathrm{t})}{\bar{\mathrm{t}}} \tag{6}$$

The term on the right-hand side is equal to the bias in the conventional mean. The two means are only equal when $\mathrm{Cov}(\mathrm{m},\mathrm{t}) = 0$. For a fixed covariance, the smaller the mean TF of the ROI, corresponding to higher partial volume, the larger the bias. The bias in the conventional mean is positive when there is a negative correlation between m and t and vice versa for positive correlation.

3. Materials and methods

3.1. Image acquisition

We analysed data acquired in a study of YOAD (Slattery et al 2017, Parker et al 2018). Ethical approval was obtained from the National Hospital for Neurology and Neurosurgery Research Ethics Committee and written informed consent obtained from all the participants. A multi-shell DWI sequence optimised for NODDI was acquired for twenty-one healthy controls and thirty YOAD patients matched for age and sex on a 3T Siemens Magnetom Trio scanner (Siemens, Erlangen, Germany) using a 32-channel phased array receiver head coil. DWI acquisitions consisted of a spin-echo echo planar imaging (EPI) sequence with EPI factor 96; TR=7000ms; TE=92ms; 55 interleaved slices with slice thickness 2.5mm; in plane FOV 240x240mm^2 with resolution 2.5x2.5mm^2; multi-slice acceleration factor 2; b-values=0 (n=13), 300 (n=8), 700 (n=32) and 2000 (n=64) s/mm^2. Optimised gradient directions from the Camino software package generated using electrostatic energy minimisation were used (Cook et al 2007). Sequences utilized twice-refocused spin echo to minimize distortion effects from eddy-currents (Reese et al 2003). The total acquisition time was 16m13s.

T1-weighted images and B0 field maps were acquired to correct for susceptibility-induced off-resonance fields. T1-weighted images were acquired using a 3D sagittal MPRAGE volumetric sequence with TE=2.9ms; TI=900ms; TR=2200ms, matrix size 256x256x208 and isotropic 1.1x1.1x1.1mm^3 voxels. For B0 field mapping, 2D dual echo

gradient echo images were acquired using an EPI sequence with TEs=4.92/7.38ms and TR=688ms, matrix size 64x64x55 and resolution 3x3x3mm^3.

3.2. Pre-processing

DWI non-brain voxels were removed by aligning the intracranial volume mask of the T1-weighted image to the DWI using SPM12 (Malone et al 2015). Inter-volume misalignment due to motion and image distortions due to residual eddy current-induced off-resonance fields were corrected using FSL eddy v6.0.2 (Jenkinson et al 2012, Andersson et al 2016). B0 maps were calculated from the unwrapped gradient echo phase images. Distortions in the DWIs due to susceptibility-induced off-resonance fields were corrected via a combined approach using the B0 maps and registration to the T1-weighted image (Daga et al 2014).

3.3. NODDI metrics

The NODDI model was fitted to the pre-processed DWIs using AMICO (Zhang, H. et al 2012, Daducci et al 2015), outputting parameter maps of NDI, ODI and FWF. TF maps were calculated from the FWF as 1-FWF using FSL fslmaths.

3.4. Atlas-based parcellation of white matter ROIs

NODDI maps were parcellated into forty-eight white matter ROIs defined in the John Hopkins University (JHU) white matter atlas (Mori et al 2008), using atlas-based parcellation. This was achieved by aligning the JHU atlas with subjects' NODDI data, the latter being aligned to a bootstrapped population template (as in Zhang, J. et al 2018). The population template was created using an iterative alignment algorithm (Guimond et al 2000, Zhang, H. et al 2007, Zhang, H. et al 2010) that employs diffusion tensor (DT)-based registration in DTI-TK (Zhang, H. et al 2006), an approach shown to improve alignment in white matter (Pecheva et al 2017) and reduce systematic errors compared to FA-based registration (Keihaninejad et al 2013). The JHU Atlas was propagated to the population template via the IIT template (Zhang, S. & Arfanakis 2011), which corrects the JHU atlas for non-linear anatomical variation among the atlas participants.

ROIs were classified as periventricular (those sharing a border with ventricles, n=29) and non-periventricular (n=19) by manually inspecting ROIs overlayed on the between-subject average DT mean diffusivity maps. ROIs are shown in Fig. S1 and abbreviations are described in Table A1.

3.5. Conventional and tissue-weighted means

The conventional and tissue-weighted NDI and ODI means were calculated for all white matter ROIs for each subject. Conventional means were computed using FSL fslstats. Tissue-weighted means were computed using the implementation available at https://github.com/tdveale/NODDI-tissue-weighting-tool, which is based on the alternative formula defined in equation (3). This formula can be readily implemented with FSL fslmaths and fslstats.

3.6. Mean tissue fractions

To understand the relation between the conventional mean and CSF partial volume contamination, mean TFs were analysed for all ROIs in control and YOAD subjects by calculating their between-subject mean and standard deviation. Differences in mean TF were determined using two-tailed Welch's t-tests, a variant of the students t-test that accounts for unequal variance between groups. A Bonferroni-corrected *p*-value threshold of <0.05 was applied to determine significant differences and control family-wise error (FWE) rate to <0.05. R v3.6.1 was used for these calculations and all subsequent analyses.

3.7. Bias in conventional mean

Bias in the conventional mean was estimated in all ROIs by subtracting the tissue-weighted mean from the conventional mean. The calculated bias was equal to its theoretically predicted value $-\mathrm{Cov}(\mathrm{m},\mathrm{t})/\bar{\mathrm{t}}$ (see equation (6)).

Regional bias was summarised in control and YOAD subjects by their between-subject mean and standard deviation. Non-zero bias was determined using two-tailed one sample t-tests and the difference in bias between control and YOAD subject was determined using two-tailed Welch's t-tests. Bonferroni-corrected $p<0.05$ were considered significant.

Pearson correlation was used to test for associations between mean TF and magnitudes of bias for control and YOAD groups and two-tailed Welch's t-tests were used to test for different magnitudes of bias between periventricular and non-periventricular ROIs. In both cases $p<0.05$ was considered significant.

3.8. Group differences comparison

To determine the implications of applying the tissue-weighted mean for group differences, Cohen's d_s effect sizes (Cohen 1988), which describe the standardised mean difference between two groups of sample observations, were computed for each ROI (mean difference contrast of control minus YOAD) and compared between the conventional and

tissue-weighted mean. Two-tailed Welch's t-tests were used to determine significant group differences. Bonferroni-corrected $p<0.05$ were considered significant.

4. Results

4.1. Mean tissue fractions

Mean TF varied between regions (Fig. 3) and as expected, tended to be lower in periventricular regions (Table A1), suggesting those ROIs experienced higher CSF partial volume contamination. YOAD subjects ROIs tended to have lower mean TFs than control subjects, consistent with expected increases in CSF partial volume contamination due to atrophy.

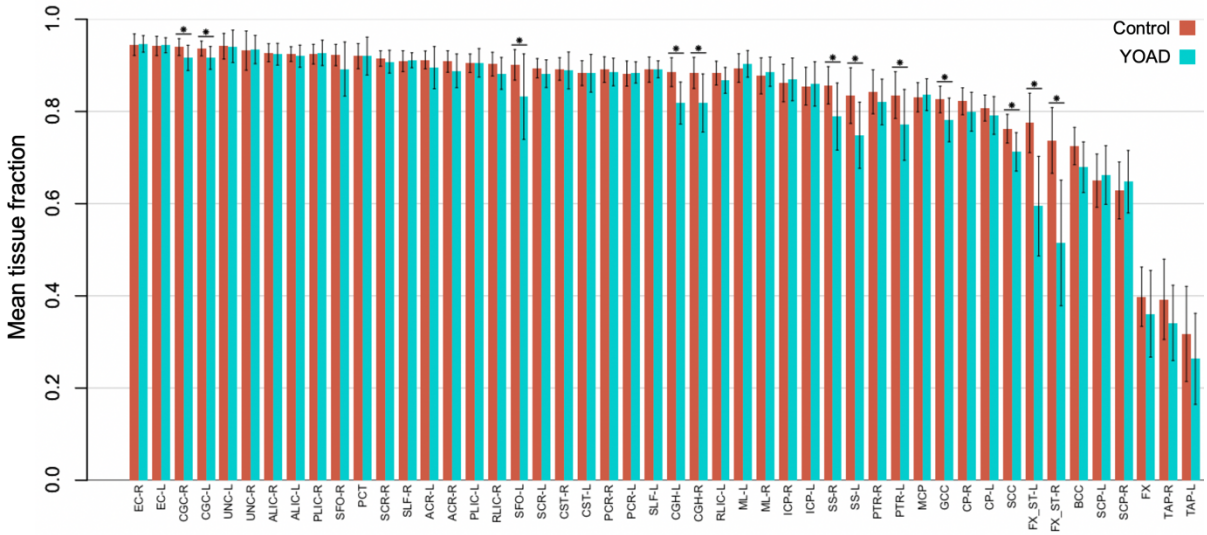

Figure 3. Mean TFs in control and YOAD subjects for all white matter ROIs. Bars show the mean ± standard deviation of the mean TF across subjects. ROIs are in decreasing order of mean TF in control subjects from left to right. Bilateral ROIs are ordered adjacently when no significant difference was observed by two-tailed t-test between their mean TFs in control subjects. Horizontal lines with stars denote significantly lower mean TF in YOAD subjects, determined using two-sided Welch's t-tests ($p<0.05$ Bonferroni-corrected across ROIs).

4.2. Bias in the conventional mean

There was statistically significant evidence of bias in the conventional mean of NODDI metrics for most brain ROIs (Fig. 4). Those with lower mean TF tended to have higher magnitudes of bias (Fig. 5), as expected from equation (6) – the correlation between

mean magnitude of bias and the inverse of mean TF was 0.95 for NDI in controls (p=8.9x10^{-25}), 0.89 for NDI in YOAD (p=5.7x10^{-17}), 0.98 for ODI in controls (p=8.2x10^{-35}) and 0.97 for ODI in YOAD (6.2x10^{-30}). As implied, YOAD subjects' ROIs with relatively lower mean TF tended to display greater bias.

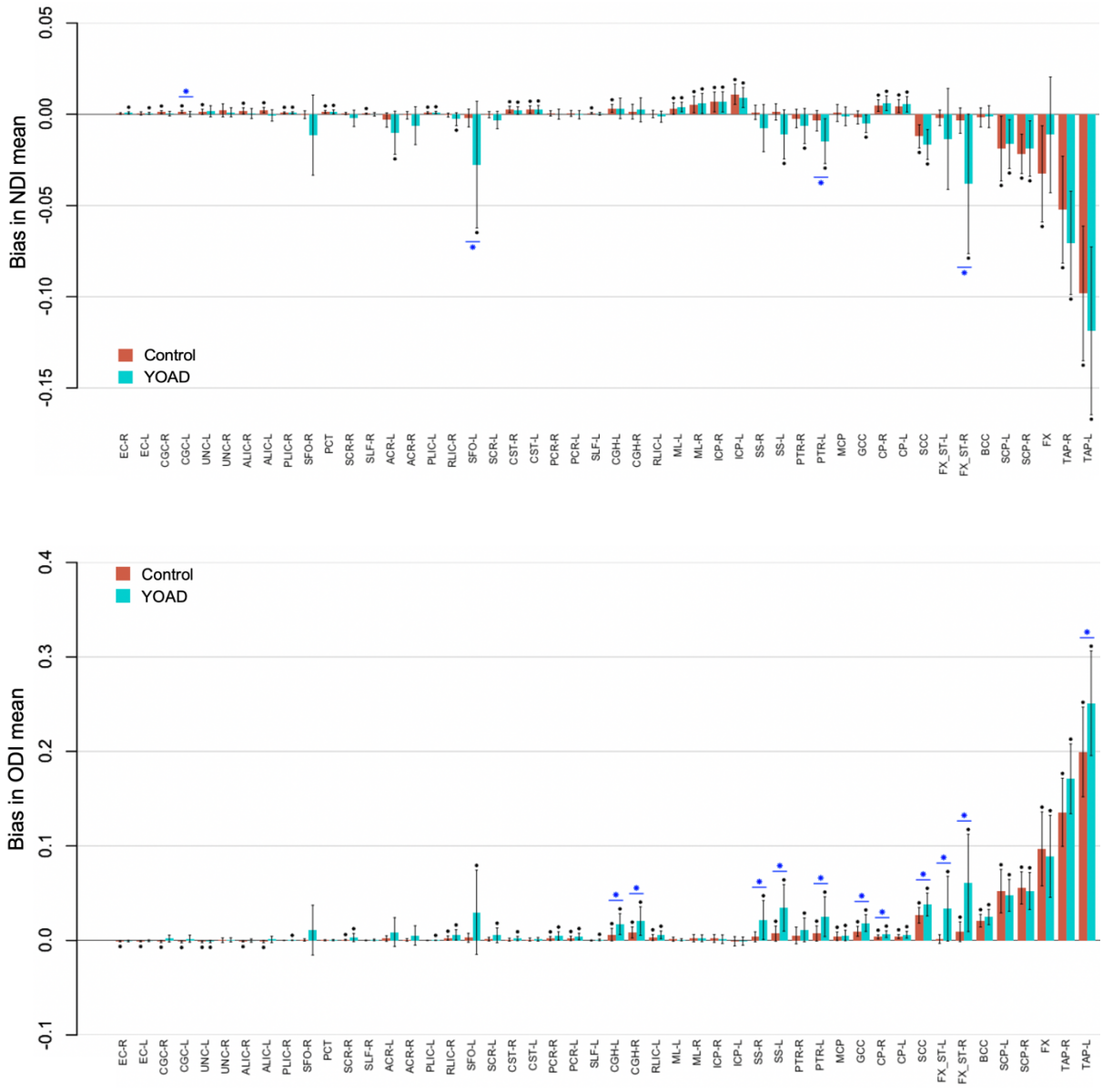

Figure 4. Bias in conventional means for all white matter ROIs. Bars show the mean ± standard deviation of bias across subjects. The height of each bar is the average bias across subjects, equal to the bias in the group mean. Black stars indicate significant evidence of non-zero bias, determined using two-sided one sample t-tests (p<0.05 Bonferroni-corrected across ROIs). Blue stars indicate significant differences in bias between control and YOAD subjects, determined using two-sided Welch's t-tests (p<0.05 Bonferroni-corrected across ROIs). ROIs are ordered as in Fig. 3.

Periventricular ROIs tended to have higher magnitudes of bias than non-periventricular ROIs. Significantly higher bias for ODI in control subjects (p=0.018) and YOAD subjects (p=0.011) was observed for periventricular ROIs, whereas NDI bias tended to be higher in periventricular ROIs for both groups, but was not significant (control p=0.053, YOAD p=0.072).

NDI tended to be negatively biased (under-estimated) and ODI positively biased (over-estimated), an effect more pronounced in ROIs with lower mean TF. This directionality reflects the sign of their covariance (Fig. 5).

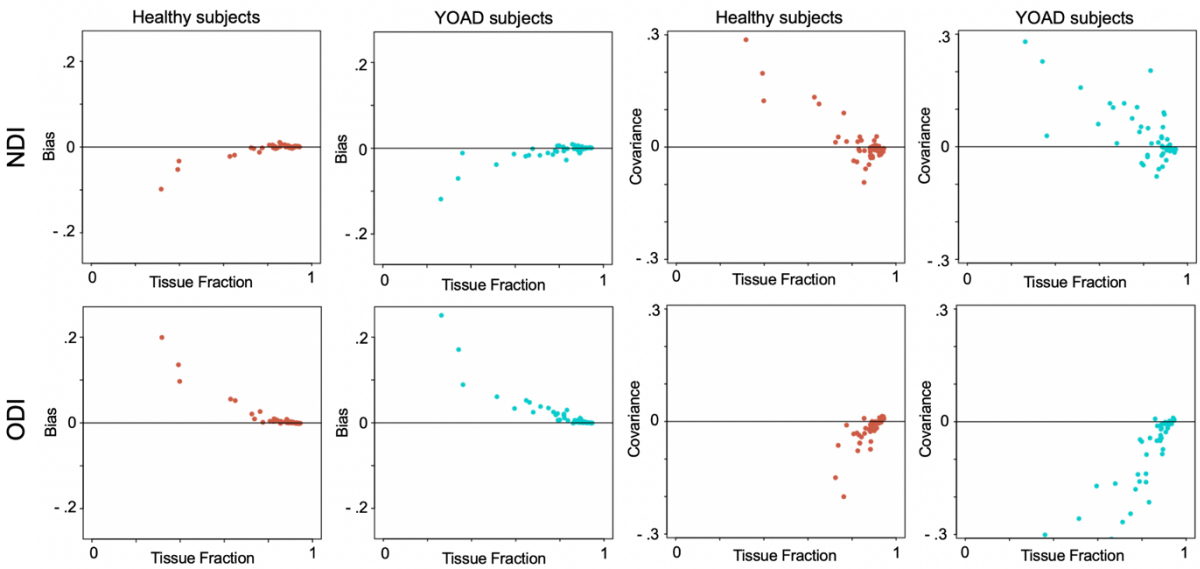

Figure 5. Relation between ROI mean TF, bias in the conventional mean and covariance between microstructure metrics and TF, plotted for NDI and ODI for each white matter ROI in control and YOAD subjects. Each dot shows the between-subject average of the ROI mean.

4.3. Group differences comparison

Fig. 6 compares the estimated effect sizes computed using the conventional mean (Fig. S2) and tissue-weighted mean (Fig. S3) for all ROIs. Overall, effect sizes were similar using the two approaches, with only small differences observed for the majority of ROIs. However, those ROIs with large differences in bias between control and YOAD groups (Fig. 4) tended to have large differences in effect sizes.

Using the conventional mean, effect sizes for lower NDI in YOAD compared to controls were slightly over-estimated in comparison to the tissue-weighted mean for most

ROIs (25/39 showing lower NDI, Fig. 6a), with the largest over-estimation observed for the left tapetum (L-TAP) and superior frontal occipital fasciculus (L-SFO). In these ROIs, bias was higher in the group means of the YOAD group than in controls. However, for 14 ROIs in which bias was higher in the group mean of controls, effect sizes for lower NDI in YOAD were under-estimated using the conventional mean. This resulted in a gain of significant group differences for reduced NDI in the fornix (FX) using the tissue-weighted mean ($p<0.05$, Bonferroni-corrected).

Effect sizes for lower ODI in YOAD were under-estimated for most ROIs (18/23 with lower ODI) using the conventional mean (Fig. 6b). This was due to higher ODI bias in the mean of YOAD groups than in controls. The tissue-weighted mean resulted in a gain of significant group differences for lower ODI in YOAD in the left posterior corona radiata (L-PCR) which was absent using the conventional mean. There were also ROIs with over-estimated effect sizes for higher ODI in YOAD using the conventional mean. Significant group differences for higher ODI in YOAD were absent for the right hippocampal cingulum (CGH-R) and genu of the corpus callosum (GCC) when using the tissue-weighted mean compared to the conventional mean.

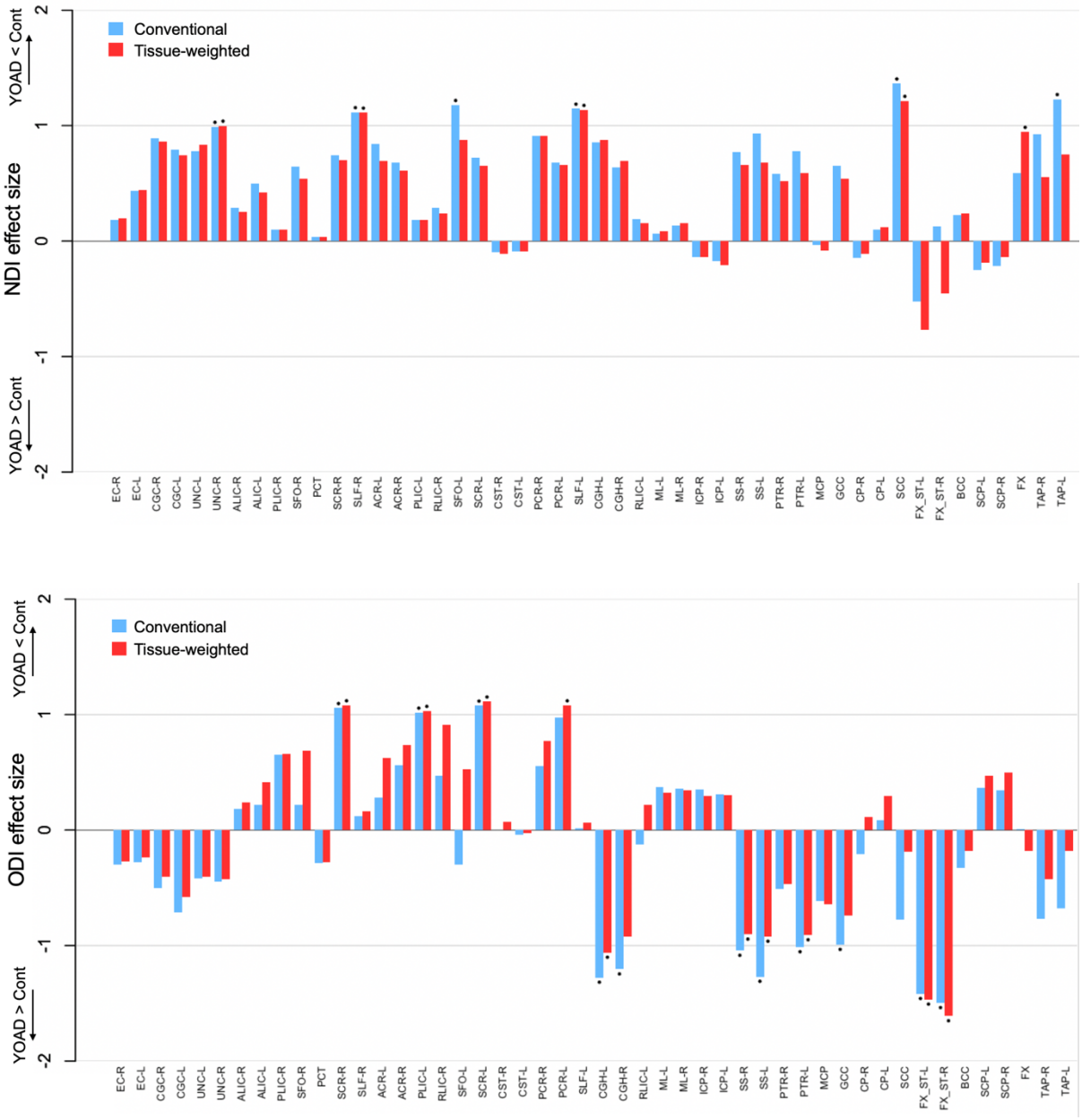

Figure 6. Effect sizes for NDI (upper) and ODI (lower) across all ROIs for group differences between control and YOAD subjects (Cohen's d_s, mean difference contrast of control minus YOAD) using the conventional mean (blue) and tissue-weighted mean (red). Positive effect sizes correspond to lower means in YOAD subjects and negative effect sizes to higher means in YOAD subjects. Stars indicate significant differences between the control and YOAD group as determined by two-tailed Welch's t-tests on the group means (p<0.05 Bonferroni-corrected across ROIs). ROIs are ordered as in Fig. 3.

5. Discussion

This study introduces the tissue-weighted mean, an unbiased method for estimating the mean of NODDI tissue microstructure metrics within an ROI. We observed statistically significant bias in conventional means for most ROIs and an association between higher magnitudes of bias and lower tissue fraction. Furthermore, the observed bias confounds the estimation of group differences, resulting in effect sizes of conventional means being either over- or under-estimated compared to the tissue-weighted mean.

Bias in conventional means occurs because the contribution of voxels with low TF are over-weighted. Periventricular ROIs, which tended to have lower mean TF consistent with CSF partial volume contamination, had higher magnitudes of bias. These findings suggest that in general the periventricular structures, such as the corpus callosum, are particularly susceptible to bias. Certain small periventricular structures, such as the tapetum and fornix, appear even more susceptible due to the relatively high proportion of their surface bordering CSF and larger surface area to volume ratio. Furthermore, as brain atrophy leads to reduced regional volumes and enlarged ventricles (Vernooij et al 2008, Agosta et al 2011), regions that have undergone atrophy may have an even higher propensity for bias, which is supported by findings of higher bias in the YOAD group.

Bias in conventional means impacted estimation of group differences. Effect sizes computed using the conventional mean were either under- or over-estimated (Fig. 6). The magnitude of effect size mis-estimation was region-dependent, with ROIs that had higher differences in bias magnitudes between groups also having higher differences in effect sizes. Effect sizes in structures containing substantial partial volume tended to be more severely affected. These results suggest that bias in conventional means can confound estimation of effect sizes in group studies.

In this exemplar application of the tissue-weighted mean in a study of YOAD, we observed a high concordance of significant group differences to expected regional pathology, demonstrating that the tissue-weighted mean is sensitive to biologically plausible disease effects. For instance, the tissue-weighted mean found significantly lower NDI, consistent with tissue neurodegeneration, in the fornix (FX), which was absent using the conventional mean. Increased ODI was observed in bilateral fornix/stria terminalis (FX_ST-L/R) and left hippocampal cingulum ROIs (CGH-L). These regions form hippocampal connections involved in memory processing (Mielke et al 2012, Dubois et al 2016), a brain function associated with symptoms of Alzheimer's disease and YOAD (Rossor et al 2010).

The confounding influence of bias on estimation of effect sizes suggests previous studies in neurodegenerative diseases that use conventional ROI means of NODDI tissue metrics to investigate microstructure differences in periventricular regions and those

undergoing atrophy should be interpreted with caution. Firstly, our study suggests that some true disease effects can be masked by bias, as evidenced by ROIs that had higher effect sizes when using the tissue-weighted mean compared to the conventional mean. Secondly, the conventional mean may have over-estimated the effect sizes for some ROIs in previous work. For example, a recent tract-specific study in mild cognitive impairment found changes in NODDI tissue metrics in the hippocampal cingulum in human subjects (Wen, Q. et al 2019). Altered microstructure in the corpus callosum using NODDI has also been reported in animal models of Alzheimer's disease (Colgan et al 2016). Although the direction of metric changes in these regions are consistent with neurodegeneration, our study suggests the effects reported may have been over-estimated.

6. Conclusion

This study shows bias in conventional ROI means is prevalent and particularly affects periventricular regions where partial volume due to CSF contamination is higher. This bias confounds group difference metrics, suggesting previous studies using the conventional means should be interpreted with caution. The proposed tissue-weighted mean provides unbiased estimation of regional mean NODDI tissue metrics of tissue microstructure. It can be used to accurately identify disease effects in future studies of white matter neurodegeneration, especially for periventricular regions and for other brain tissues prone to CSF contamination, such as cortical grey matter. This may provide additional insight into mechanisms of brain behaviour associations in aging, development and neurodegeneration.

Acknowledgments

CP and GZ were funded by the Wellcome Trust (Collaborative Award 200181/Z/15/Z). TV was funded by an Alzheimer's Research UK PhD scholarship (ARUK-PhD2018-009). MB was supported by a Fellowship award from the Alzheimer's Society, UK (AS-JF-19a-004-517). MB's work was also supported by the UK Dementia Research Institute which receives its funding from DRI Ltd, funded by the UK Medical Research Council, Alzheimer's Society and Alzheimer's Research UK. IM was supported by Alzheimer's Research UK (ARUK-PG2014–1946, ARUK-PG2017–1946) and the Wolfson Foundation (PR/ylr/18575). DLT was supported by the UCL Leonard Wolfson Experimental Neurology Centre (PR/ylr/18575), UCLH NIHR Biomedical Research Centre and the Wellcome Trust (Centre award 539208). JMS acknowledges the support of the National Institute for Health Research University College London Hospitals Biomedical Research Centre, Wolfson Foundation, Alzheimer's Research UK, Brain Research UK, Weston Brain Institute, Medical Research Council, British Heart Foundation, UK Dementia Research Institute and Alzheimer's Association. DMC was supported by the UK Dementia Research Institute which receives its funding from DRI Ltd, funded by the UK Medical Research Council, Alzheimer's Society and Alzheimer's Research UK, as well as Alzheimer's Research UK (ARUK-PG2017-1946) and the UCL/UCLH NIHR Biomedical Research Centre. We would also like to acknowledge Prof. Nick Fox who is a senior NIHR investigator for his role in conceiving the initial YOAD study preceding this work.

The authors would like to thank all research participants who made this study possible, as well as Alzheimer's Research UK and Iceland Foods Charitable Foundation for funding the Young-Onset Alzheimer's disease study. The Dementia Research Centre is supported by Alzheimer's Research UK, Brain Research Trust, and The Wolfson Foundation. They also thank Kirsty Lu, Amelia Carton, Timothy Shakespeare, Keir Yong, Aida Suarez Gonzalez and Silvia Primativo for assistance with neuropsychology assessments.

References

1. Agosta, F., Pievani, M., Sala, S., Geroldi, C., Galluzzi, S., Frisoni, G. B. & Filippi, M. White matter damage in Alzheimer disease and its relationship to gray matter atrophy. *Radiology* 258, 853–863 (2011).
2. Alexander, D. C., Dyrby, T. B., Nilsson, M. & Zhang, H. Imaging brain microstructure with diffusion MRI: practicality and applications. *NMR in Biomedicine* 32, e3841 (2019).
3. Andersson, J. L. & Sotiropoulos, S. N. An integrated approach to correction for off-resonance effects and subject movement in diffusion MR imaging. *Neuroimage* 125, 1063–1078 (2016).
4. Andica, C., Kamagata, K., Hatano, T., Saito, A., Uchida, W., Ogawa, T., Takeshige-Amano, H., Zalesky, A., Wada, A., Suzuki, M., Hagiwara, A., Irie, R., Hori, M., Kumamaru, K. K., Oyama, G., Shimo, Y., Umemura, A., Pantelis, C., Hattori, N. & Aoki, S. Free-water imaging in white and gray matter in Parkinson's disease. *Cells* 8, 839 (2019).
5. Andica, C., Kamagata, K., Hatano, T., Saito, Y., Ogaki, K., Hattori, N. & Aoki, S. MR biomarkers of degenerative brain disorders derived from diffusion imaging. *Journal of Magnetic Resonance Imaging* 52, 1620–1636 (2020).
6. Broad, R. J., Gabel, M. C., Dowell, N. G., Schwartzman, D. J., Seth, A. K., Zhang, H., Alexander, D. C., Cercignani, M. & Leigh, P. N. Neurite orientation and dispersion density imaging (NODDI) detects cortical and corticospinal tract degeneration in ALS. *Journal of Neurology, Neurosurgery & Psychiatry* 90, 404–411 (2019).
7. Cohen, J. Statistical power analysis for the behavioral sciences 1988.
8. Colgan, N., Siow, B., O'Callaghan, J. M., Harrison, I. F., Wells, J. A., Holmes, H. E., Ismail, O., Richardson, S, Alexander, D. C., Collins, E. C., Fisher, E. M., Johnson, R., Schwarz, A. J., Ahmed, Z., O'Neil, M. J., Murray, T. K., Zhang, H., Lythgoe, M. Application of neurite orientation dispersion and density imaging (NODDI) to a tau pathology model of Alzheimer's disease. *Neuroimage* 125, 739–744 (2016).
9. Cook, P. A., Symms, M., Boulby, P. A. & Alexander, D. C. Optimal acquisition orders of diffusion-weighted MRI measurements. *Journal of Magnetic Resonance Imaging* 25, 1051–1058 (2007).
10. Daducci, A., Canales-Rodriguez, E. J., Zhang, H., Dyrby, T. B., Alexander, D. C. & Thiran, J.P. Accelerated microstructure imaging via convex optimization (AMICO) from diffusion MRI data. *Neuroimage* 105, 32–44 (2015).
11. Daga, P., Pendse, T., Modat, M., White, M., Mancini, L., Winston, G. P., McEvoy, A. W., Thornton, J., Yousry, T., Drobnjak, I., Duncan, J. S. Susceptibility artefact correction using dynamic graph cuts: application to neurosurgery. Medical image analysis 18, 1132–1142 (2014).
12. Dubois, B., Hampel, H., Feldman, H. H., Scheltens, P., Aisen, P., Andrieu, S., Bakardjian, H., Benali, H., Bertram, L., Blennow, K., Broich, K., Cavedo, E., Crutch, S., Dartigues, J.F., Duyckaerts, C., Epelbaum, S., Frisoni, G. B., Gauthier, S., Genthon, R., Gouw, A. A., Habert, M.O., Holtzman, D. M., Kivipelto, M., Lista, S., Molinuevo, J.L., O'Bryant, S. E., Rabinovici, G. D., Rowe, C., Salloway, S., Schneider, L. S., Sperling, R., Teichmann, M., Carrillo, M. C., Cummings, J. & Jack, C. R. Preclinical Alzheimer's disease: definition, natural history, and diagnostic criteria. *Alzheimer's & Dementia* 12, 292–323 (2016).
13. Genc, E., Fraenz, C., Schluter, C., Friedrich, P., Hossiep, R., Voelkle, M. C., Ling, J. M., Gunturkun, O. & Jung, R. E. Diffusion markers of dendritic density and arborization in gray matter predict differences in intelligence. *Nature communications* 9, 1–11 (2018).
14. Guimond, A., Meunier, J. & Thirion, J.P. Average brain models: A convergence study. Computer vision and image understanding 77, 192– 210 (2000).
15. Jenkinson, M., Beckmann, C. F., Behrens, T. E., Woolrich, M. W. & Smith, S. M. Fsl. *Neuroimage* 62, 782–790 (2012)
16. Keihaninejad, S., Zhang, H., Ryan, N. S., Malone, I. B., Modat, M., Cardoso, M. J., Cash, D. M., Fox, N. C. & Ourselin, S. An unbiased longitudinal analysis framework for tracking white matter changes using diffusion tensor imaging with application to Alzheimer's disease. *Neuroimage* 72, 153–163 (2013).
17. Kodiweera, C., Alexander, A. L., Harezlak, J., McAllister, T. W. & Wu, Y.C. Age effects and sex differences in human brain white matter of young to middle-aged adults: A DTI, NODDI, and q-space study. *Neuroimage* 128, 180–192 (2016).
18. Kunz, N., Zhang, H., Vasung, L., O'Brien, K. R., Assaf, Y., Lazeyras, F., Alexander, D. C. & Huppi, P. S. Assessing white matter microstructure of the newborn with multi-shell diffusion MRI and biophysical compartment models. *Neuroimage* 96, 288–299 (2014).

19. Lynch, K. M., Cabeen, R. P., Toga, A. W. & Clark, K. A. Magnitude and timing of major white matter tract maturation from infancy through adolescence with NODDI. *NeuroImage* 212, 116672 (2020).
20. Malone, I. B., Leung, K. K., Clegg, S., Barnes, J., Whitwell, J. L., Ashburner, J., Fox, N. C. & Ridgway, G. R. Accurate automatic estimation of total intracranial volume: a nuisance variable with less nuisance. Neuroimage 104, 366–372 (2015).
21. Metzler-Baddeley, C., O'Sullivan, M. J., Bells, S., Pasternak, O. & Jones, D. K. How and how not to correct for CSF-contamination in diffusion MRI. *Neuroimage* 59, 1394–1403 (2012).
22. Mielke, M. M., Okonkwo, O. C., Oishi, K., Mori, S., Tighe, S., Miller, M. I., Ceritoglu, C., Brown, T., Albert, M. & Lyketsos, C. G. Fornix integrity and hippocampal volume predict memory decline and progression to Alzheimer's disease. *Alzheimer's & Dementia* 8, 105–113 (2012).
23. Mollink, J., Smith, S. M., Elliott, L. T., Kleinnijenhuis, M., Hiemstra, M., Alfaro-Almagro, F., Marchini, J., van Walsum, A.M. v. C., Jbabdi, S. & Miller, K. L. The spatial correspondence and genetic influence of interhemispheric connectivity with white matter microstructure. *Nature neuroscience* 22, 809–819 (2019).
24. Mori, S., Oishi, K., Jiang, H., Jiang, L., Li, X., Akhter, K., Hua, K., Faria, A. V., Mahmood, A., Woods, R., Toga, A. W., Pike, G. B., Neto, P. R., Evans, A., Zhang, J., Huang, H., Miller, M. I., van Zijl, P. & Mazziotta, J. Stereotaxic white matter atlas based on diffusion tensor imaging in an ICBM template. *NeuroImage* 40, 570–582 (2008).
25. Parker, T. D., Slattery, C. F., Zhang, J., Nicholas, J. M., Paterson, R. W., Foulkes, A. J., Malone, I. B., Thomas, D. L., Modat, M., Cash, D. M., Crutch, S. J., Alexander, D. C., Ourselin, S., Fox, N. C., Zhang, H. & Schott, J. M. Cortical microstructure in young onset Alzheimer's disease using neurite orientation dispersion and density imaging. *Human brain mapping* 39, 3005–3017 (2018).
26. Pecheva, D., Yushkevich, P., Batalle, D., Hughes, E., Aljabar, P., Wurie, J., Hajnal, J. V., Edwards, A. D., Alexander, D. C., Counsell, S. J., Zhang, H. A tract-specific approach to assessing white matter in preterm infants. *Neuroimage* 157, 675–694 (2017).
27. Reese, T. G., O. Heid, R. M. Weisskoff & V. J. Wedeen. Reduction of eddy-current-induced distortion in diffusion MRI using a twice-refocused spin echo. *Magnetic Resonance in Medicine*. 49, 177-182 (2003)
28. Rossor, M. N., Fox, N. C., Mummery, C. J., Schott, J. M. & Warren, J. D. The diagnosis of young-onset dementia. *The Lancet Neurology* 9, 793–806 (2010).
29. Scahill, R. I., Zeun, P., Osborne-Crowley, K., Johnson, E. B., Gregory, S., Parker, C., Lowe, J., Nair, A., O'Callaghan, C., Langley, C., Papoutsi, M., McColgan, P., Estevez-Fraga, C., Fayer, K., Wellington, H., Rodrigues, F. B., Byrne, L. M., Heselgrave, A., Hyare, H., Sampaio, C., Zetterberg, H., Zhang, H., Wild, E. J., Rees, G., Robbins, T. W., Sahakian, B. J., Langbehn, D. & Tabrizi, S. J. Biological and clinical characteristics of gene carriers far from predicted onset in the Huntington's disease Young Adult Study (HD-YAS): a cross-sectional analysis. *The Lancet Neurology* 19, 502–512 (2020).
30. Slattery, C. F., Zhang, J., Paterson, R. W., Foulkes, A. J., Carton, A., Macpherson, K., Mancini, L., Thomas, D. L., Modat, M., Toussaint, N., Cash, D. M., Thornton, J. S., Henley, S. M., Crutch, S. J., Alexander, D. C., Ourselin, S., Fox, N. C., Zhang, H., Schott, J. M. ApoE influences regional white-matter axonal density loss in Alzheimer's disease. *Neurobiology of aging* 57, 8–17 (2017).
31. Veale, T., Malone, I. B., Poole, T., Parker, T. D., Slattery, C. F., Paterson, R. W., Foulkes, A. J., Thomas, D. L., Schott, J. M., Zhang, H., Fox, N. C. Loss and Reorganisation of Superficial White Matter in Alzheimer's disease: A Diffusion MRI study. Preprint in medRxiv (May 2021). https://doi.org/10.1101/2021.05.07.21256728
32. Vernooij, M. W., de Groot, M., van der Lugt, A., Ikram, M. A., Krestin, G. P., Hofman, A., Niessen, W. J. & Breteler, M. M. White matter atrophy and lesion formation explain the loss of structural integrity of white matter in aging. *Neuroimage* 43, 470–477 (2008).
33. Vos, S. B., Jones, D. K., Viergever, M. A. & Leemans, A. Partial volume effect as a hidden covariate in DTI analyses. *Neuroimage* 55, 1566–1576 (2011).
34. Wen, J., Zhang, H., Alexander, D. C., Durrleman, S., Routier, A., Rinaldi, D., Houot, M., Couratier, P., Hannequin, D., Pasquier, F., Zhang, J., Colliot, O., Le Ber, I. & Bertrand, A. Neurite density is reduced in the presymptomatic phase of C9orf72 disease. *Journal of Neurology, Neurosurgery & Psychiatry* 90, 387–394 (2019).
35. Wen, Q., Mustafi, S. M., Li, J., Risacher, S. L., Tallman, E., Brown, S. A., West, J. D., Harezlak, J., Farlow, M. R., Unverzagt, F. W., Gao, S., Apostolova, L. G., Savkin, A. J., Wu, Y. White matter alterations in early-stage Alzheimer's disease: A tract-specific study. *Alzheimer's & Dementia: Diagnosis, Assessment & Disease Monitoring* 11, 576–587 (2019).

36. Winston, G. P., Micallef, C., Symms, M. R., Alexander, D. C., Duncan, J. S. & Zhang, H. Advanced diffusion imaging sequences could aid assessing patients with focal cortical dysplasia and epilepsy. *Epilepsy research* 108, 336–339 (2014).
37. Zhang, H., Schneider, T., Wheeler-Kingshott, C. A. & Alexander, D. C. NODDI: practical in vivo neurite orientation dispersion and density imaging of the human brain. *Neuroimage* 61, 1000–1016 (2012).
38. Zhang, H., Yushkevich, P. A., Alexander, D. C. & Gee, J. C. Deformable registration of diffusion tensor MR images with explicit orientation optimization. *Medical image analysis* 10, 764–785 (2006).
39. Zhang, H., Yushkevich, P. A., Rueckert, D. & Gee, J. C. A computational white matter atlas for aging with surface-based representation of fasciculi in *International Workshop on Biomedical Image Registration* (2010), 83–90.
40. Zhang, H., Yushkevich, P. A., Rueckert, D. & Gee, J. C. Unbiased white matter atlas construction using diffusion tensor images in *International conference on medical image computing and computer-assisted intervention* (2007), 211–218.
41. Zhang, J., Gregory, S., Scahill, R. I., Durr, A., Thomas, D. L., Lehericy, S., Rees, G., Tabrizi, S. J., Zhang, H. & TrackOn-HD investigators. In vivo characterization of white matter pathology in premanifest huntington's disease. *Annals of neurology* 84, 497–504 (2018).
42. Zhang, S & Arfanakis, K. Investigating the role of ICBM-space human brain diffusion tensor templates in inter-subject spatial normalization in *Proc. Intl. Soc. Mag. Reson. Med* 19 (2011), 344.

Appendix

Table A1. JHU atlas white matter ROI location, abbreviations and region names.

Periventricular	
MCP	Middle cerebellar peduncle
GCC	Genu of corpus callosum
BCC	Body of corpus callosum
SCC	Splenium of corpus callosum
FX	Fornix
ML-R	Medial lemniscus right
ML-L	Medial lemniscus left
SCP-R	Superior cerebellar peduncle right
SCP-L	Superior cerebellar peduncle left
CP-R	Cerebral peduncle right
CP-L	Cerebral peduncle left
ALIC-R	Anterior limb of internal capsule right
ALIC-L	Anterior limb of internal capsule left
RLIC-R	Retrolenticular part of internal capsule right
RLIC-L	Retrolenticular part of internal capsule left
ACR-R	Anterior corona radiata right
ACR-L	Anterior corona radiata left
PCR-R	Posterior corona radiata right
PCR-L	Posterior corona radiata left
SS-R	Sagittal stratum right
SS-L	Sagittal stratum left
EC-R	External capsule right
EC-L	External capsule left
CGH-R	Cingulum (hippocampus) right
CGH-L	Cingulum (hippocampus) left
FX-ST-R	Fornix or stria-terminalis right
FX-ST-L	Fornix or stria-terminalis left
TAP-R	Tapetum right
TAP-L	Tapetum left
Non-Periventricular	
PCT	Pontine crossing tract
CST-R	Corticospinal tract right
CST-L	Cortical spinal tract left
ICP-R	Inferior cerebellar peduncle right
ICP-L	Inferior cerebellar peduncle left
PLIC-R	Posterior limb internal capsule right
PLIC-L	Posterior limb internal capsule left
SCR-R	Superior corona radiata right
SCR-L	Superior corona radiata left
PTR-R	Posterior thalamic radiation right
PTR-L	Posterior thalamic radiation left
CGC-R	Cingulum right
CGC-L	Cingulum left
SLF-R	Superior longitudinal fasciculus right
SLF-L	Superior longitudinal fasciculus left
SFO-R	Superior frontal occipital fasciculus right
SFO-L	Superior frontal occipital fasciculus left
UNC-R	Uncinate fasciculus right
UNC-L	Uncinate fasciculus left